Computers and Structures 157 (2015) 209–217

Contents lists available at ScienceDirect

Computers and Structures

journal homepage: www.elsevier.com/locate/compstruc

Harmonic oscillations of a thin lamina in a quiescent viscous fluid: A numerical investigation within the framework of the lattice Boltzmann method

Alessandro De Rosis *, Emmanuel Lévêque

Laboratoire de Mécanique des Fluides et d'Acoustique (LMFA), Ecole Centrale de Lyon, 36 avenue Guy de Collongue, 69134 Ecully cedex, France

ARTICLE INFO

Article history:
Received 23 April 2015
Accepted 26 May 2015
Available online 15 June 2015

Keywords:
Fluid–structure interaction
Hydrodynamic load
Lattice Boltzmann method
Immersed boundary method

ABSTRACT

The flow physics induced by the harmonic motion of a rigid thin lamina in a quiescent viscous fluid is investigated numerically by a combined lattice Boltzmann-immersed boundary approach. Consistency and accuracy are carefully examined and validated against experimental results for oscillations of small and moderate amplitudes, and against analytical predictions for zero-amplitude oscillations. Comparisons with previous lattice Boltzmann simulations highlight the benefit of the present approach in terms of accuracy. A new empirical law for the hydrodynamic function, which accounts for oscillations of large amplitudes (similar to the length of the lamina) is introduced.

© 2015 Elsevier Ltd. All rights reserved.

1. Introduction

Numerical simulations of fluid–structure interaction (FSI) phenomena attract an increasing interest from both academic and industrial researchers. Several practical applications have already been successfully investigated such as the design of micro-air vehicles [1–6], the development of underwater energy harvesting systems [7–9] and the prediction of the hydrodynamic loads acting upon the hull of a ship [10–13]. From a fundamental viewpoint, the computation of the hydrodynamic load acting upon a vibrating beam (in a quiescent viscous fluid) is a contemporary topic of special interest [14–18]. Several analytical and numerical studies have been carried out on this topic during the last decades [19–22]. More recently, several authors have discussed the effect of various parameters such as the compressibility of the flow [23], the interplay between two solid bodies [24,25], the presence of a solid wall close to the beam [26–28] or the role of a shear-dependent viscosity [29].

In [30] the frequency response of a cantilever beam immersed in a quiescent unbounded fluid has been investigated by assuming an incompressible induced flow. In particular, it is argued that the hydrodynamic load is proportional to a so-called "hydrodynamic function", which can be derived analytically for oscillations of infinitely small amplitude. In the frequency domain, the (complex-valued) hydrodynamic function possesses a real part and an imaginary part, which are proportional to the added mass and to the non-linear damping effects, respectively. Later on, Aureli et al. [31] carried out a large experimental campaign allowing them to propose a quadratic correction (in amplitude) to the imaginary part of the hydrodynamic function à la Sader, which accounts for small and moderate oscillation amplitudes. Our study is in the straight continuation of these works and extends the prediction of the hydrodynamic function to large-amplitude (similar to the length of the beam) oscillations. This regime is particularly interesting from the perspective of engineering applications and FSI mechanisms. For this purpose, simulations based on the lattice Boltzmann method have been developed.

From a computational viewpoint, it is worth noting that the present problem is highly challenging. Since the hydrodynamic function depends on the flow physics, a numerical algorithm will generate satisfactory results only if the vortex dynamics is accurately captured. Moreover, the algorithm has to preserve the impenetrability of the moving immersed body, otherwise, the flow physics is affected by remarkable errors [31,32]. Among the possible ways to predict the flow, the lattice Boltzmann (LB) method [33–35] offers a relatively new, computationally efficient and accurate alternative to the standard continuum-based approaches. The (discrete) LB method is consistent with the Navier–Stokes equations, and is second-order accurate in space and time [36]. Its numerical algorithm is relatively simple to implement and intrinsically scalable, which opens the route to complex flow simulations. In order to account for the presence of a solid body in the fluid domain, an immersed-boundary (IB) method [37–42] can be

* Corresponding author.
E-mail address: alessandro.de-rosis@ec-lyon.fr (A. De Rosis).

http://dx.doi.org/10.1016/j.compstruc.2015.05.034
0045-7949/© 2015 Elsevier Ltd. All rights reserved.

employed. Within the framework of LB simulations, the IB method has already proved itself as a relevant solution in terms of accuracy, stability and computational effort to simulate FSI phenomena [43–48].

In the present work, the LB and IB methods are combined to predict the flow induced in a quiescent viscous fluid by the harmonic oscillation of a rigid thin lamina. A particular interest has been paid to large-amplitude oscillations, for which it is expected that the tip-induced vorticity has a remarkable influence on the forces experienced by the lamina [31]. The accuracy of our numerical approach has been assessed by comparing the results with the analytical form of the hydrodynamic function proposed by [30] for vanishing oscillations, and with the empirical law given by [31] for small and moderate oscillation amplitudes. The performance of the proposed approach in terms of accuracy is proved to be superior to a previous effort carried out within the LB framework [15]. Eventually, a novel empirical expression for the hydrodynamic function is introduced, which generalizes to all amplitudes (ranging from small to large values) the previous proposal by [31].

The paper is organized as follows. In Section 2, the problem is stated. In Section 3, the numerical results are discussed. Some conclusions and perspectives are drawn in Section 4. Finally, the incidence of the grid resolution is elucidated in the Appendix, together with the role of the boundary conditions on the contour of the simulation domain.

2. Problem statement

In this section, the problem is posed and the governing equations and parameters are defined. Then, the adopted numerical strategy is recalled.

2.1. Governing equations

A rigid thin (red) lamina of length $D = 1$ m is immersed in a quiescent fluid characterized by its mass density ρ and its kinematic viscosity ν (see Fig. 1). A square unbounded fluid domain is considered, whose area is $H \times H = 25\ \mathrm{m}^2$. This lamina undergoes transverse harmonic oscillations $u(t)$ defined as

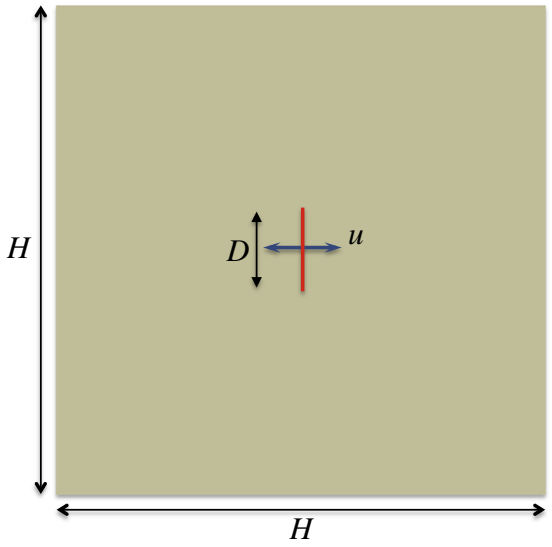

Fig. 1. Sketch of the problem set-up. A rigid (red) thin lamina of length D is immersed in a quiescent viscous fluid. It undergoes transverse harmonic oscillations $u(t)$ in time. The fluid domain is unbounded. (For interpretation of the references to color in this figure legend, the reader is referred to the web version of this article.)

$$u(t) = A \sin\left(\frac{2\pi}{T} t\right), \tag{1}$$

where t denotes the time, T and A are the period and the amplitude of the oscillations, respectively. At $t = 0$, the mid-point of the lamina is located at the center of the fluid domain. At the macroscopic level, the flow dynamics obeys the incompressible Navier–Stokes equations:

$$\nabla \cdot \mathbf{v} = 0, \tag{2}$$

$$\frac{\partial \mathbf{v}}{\partial t} + (\mathbf{v} \cdot \nabla)\mathbf{v} = -\frac{1}{\rho}\nabla p + \nu \nabla^2 \mathbf{v}, \tag{3}$$

where $\mathbf{v}$ is the flow velocity and p is the pressure field. As discussed in [14,31], the problem is governed by two dimensionless quantities, *i.e.* the frequency parameter

$$\beta = \frac{D^2}{T\nu}, \tag{4}$$

and the normalized amplitude of the oscillations $\varepsilon = A/D$. This allows us to define the Keulegan–Carpenter number $\mathcal{K} = 2\pi\varepsilon$, and the oscillatory Reynolds number $\mathcal{R} = 2\pi\beta\varepsilon$.

2.2. Numerical methods

The LB method considers the fluid at a kinetic level intermediate between the microscopic and the macroscopic. The fluid is viewed as populations of particles that collide, redistribute and propagate along the different links of a discrete lattice, so that the correct "collective" fluid dynamics (obtained by averaging over the populations of particles) are recovered at second order in the continuous limit. The LB scheme expresses the space-and-time evolution of the probability distributions of these populations on the lattice.

In the present study, the two-dimensional D2Q9 lattice is adopted [35] with the BGK (single-relaxation-time) approximation for the collision term. Namely, at position $\boldsymbol{x}$ and time t, the evolution of the distribution f_i of the particles that move with velocity $\mathbf{c}_i$ along the prescribed direction i (see Fig. 2), is given by

$$f_i(\boldsymbol{x} + \mathbf{c}_i \Delta t, t + \Delta t) = f_i(\boldsymbol{x}, t) - \frac{1}{\tau}\left[f_i(\boldsymbol{x}, t) - f_i^{eq}(\rho, \boldsymbol{v})(\boldsymbol{x}, t)\right] + Q_i \Delta t, \tag{5}$$

where Δt is the time step of the algorithm. Within the BGK approximation, the collision term expresses as a relaxation to the

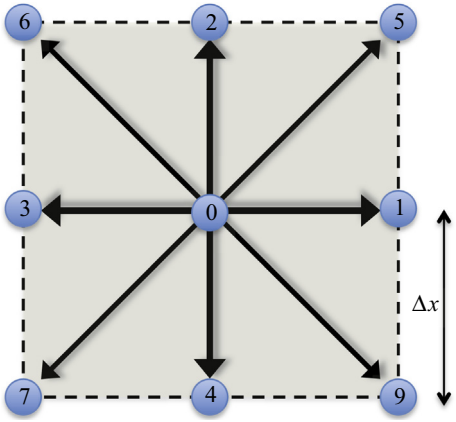

Fig. 2. The populations of particles travel from a lattice node to its nine neighbors (including the node itself) during Δt. By definition, $\Delta x/\Delta t = \sqrt{3}c_s$ where c_s can be identified with the speed of sound in the fluid.

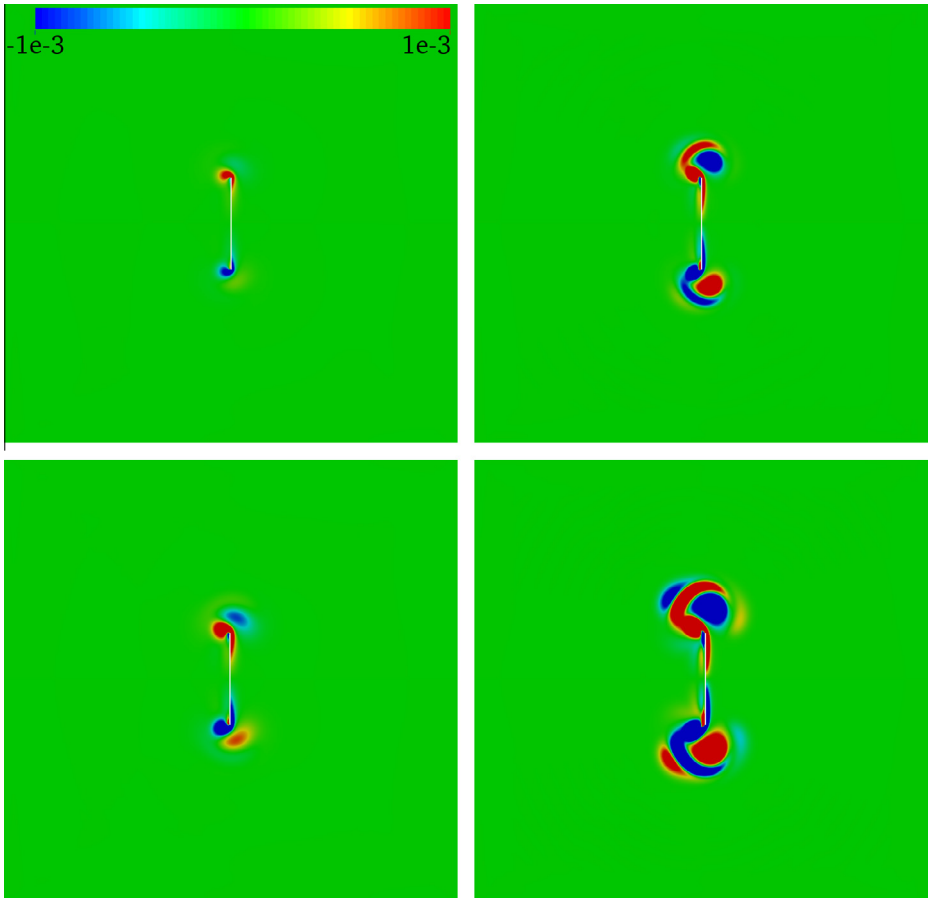

Fig. 3. Vorticity field (in lattice unit) at $t/T = 3$ for $\varepsilon = 0.075$ (top row) and $\varepsilon = 0.1$ (bottom row) at $\beta = 100$ (left column) and $\beta = 300$ (right column). The lamina is indicated by the vertical white line. The colormap is kept fixed for all the graphs and its range is reported only in the top left panel. (For interpretation of the references to color in this figure legend, the reader is referred to the web version of this article.)

equilibrium distribution $f_i^{eq}(\rho, \boldsymbol{v})$. To be compliant to the Navier–Stokes equations at the macroscopic level, this latter should be computed according to

$$f_i^{eq}(\rho, \boldsymbol{v}) = w_i \rho \left[1 + \frac{\mathbf{c}_i \cdot \boldsymbol{v}}{c_s^2} + \frac{(\mathbf{c}_i \cdot \boldsymbol{v})^2}{2c_s^4} - \frac{\boldsymbol{v} \cdot \boldsymbol{v}}{2c_s^2} \right], \tag{6}$$

where the weights $w_0 = 4/9$, $w_{1\ldots4} = 1/9$ and $w_{5\ldots8} = 1/36$, and c_s *a priori* refers to the speed of sound in the fluid [35]. The relaxation parameter τ should be related to the (kinematic) viscosity by $\nu = (\tau - 1/2)c_s^2 \Delta t$. It is worth mentioning that the LB method is intrinsically weakly compressible with the pressure being bound to the mass density by $P = c_s^2 \rho$. In order to approach the incompressible limit, c_s can be fixed at an arbitrary (non-physical) large value so that the local Mach number $\mathcal{M} = |\boldsymbol{v}|/c_s$ remains very low in the whole fluid domain, *e.g.* $\mathcal{M} < 0.05$.

The additional source term Q_i is introduced to account for the presence of the immersed solid body [49]. Within a typical time step, this term is firstly ignored and the usual collide-and-streaming scheme is performed. The macroscopic fluid density ρ and the flow velocities $\boldsymbol{v}$ are computed as usual as

$$\rho = \sum_i f_i \quad \text{and} \quad \rho \boldsymbol{v} = \sum_i f_i \mathbf{c}_i. \tag{7}$$

Then, the discrete source terme Q_i is estimated according to

$$Q_i = \left(1 - \frac{1}{2\tau}\right) w_i \left[\frac{\mathbf{c}_i - \boldsymbol{v}}{c_s^2} + \frac{(\mathbf{c}_i \cdot \boldsymbol{v})}{c_s^4} \mathbf{c}_i \right] \cdot \boldsymbol{q}, \tag{8}$$

where $\boldsymbol{q}$ represents the force (acting on the fluid) induced by the presence of the immersed body. Eventually, the distributions are updated by adding the contribution due to the IB force at the lattice node: $f_i^\star = f_i + Q_i \Delta t$, and the velocity is corrected as

$$\rho \boldsymbol{v}^\star = \sum_i f_i^\star \mathbf{c}_i + \frac{1}{2} \boldsymbol{q} \Delta t, \tag{9}$$

before proceeding the next time step. As recently stated in [50], this scheme preserves the second-order accuracy of the LB method.

The presence of the lamina (immersed in the fluid lattice) is taken into account by adopting the immersed boundary (IB) method [37,38,41]. Specifically, the lamina is idealized by a set of Lagrangian solid points, whose reciprocal spacing is set to one half of the fluid-domain mesh size. The IB is built in an implicit velocity-correction strategy, leading to the correction force $\boldsymbol{q}$ introduced above in the LB scheme. We do not recall here the details of the immersed boundary method but refers the reader to [38] for a comprehensive introduction. Interestingly, the fluid forces (acting on the immersed boundary) can be easily and immediately evaluated from the IB method as

$$\boldsymbol{F} = -\sum_{\boldsymbol{x}} \boldsymbol{q}. \tag{10}$$

Within the framework of the LB method, the IB algorithm presents some benefit over classical (interpolated) bounce-back rules to handle the presence of the oscillating lamina [15,51–54]. Firstly, the representation of the lamina as a set of *Lagrangian points*

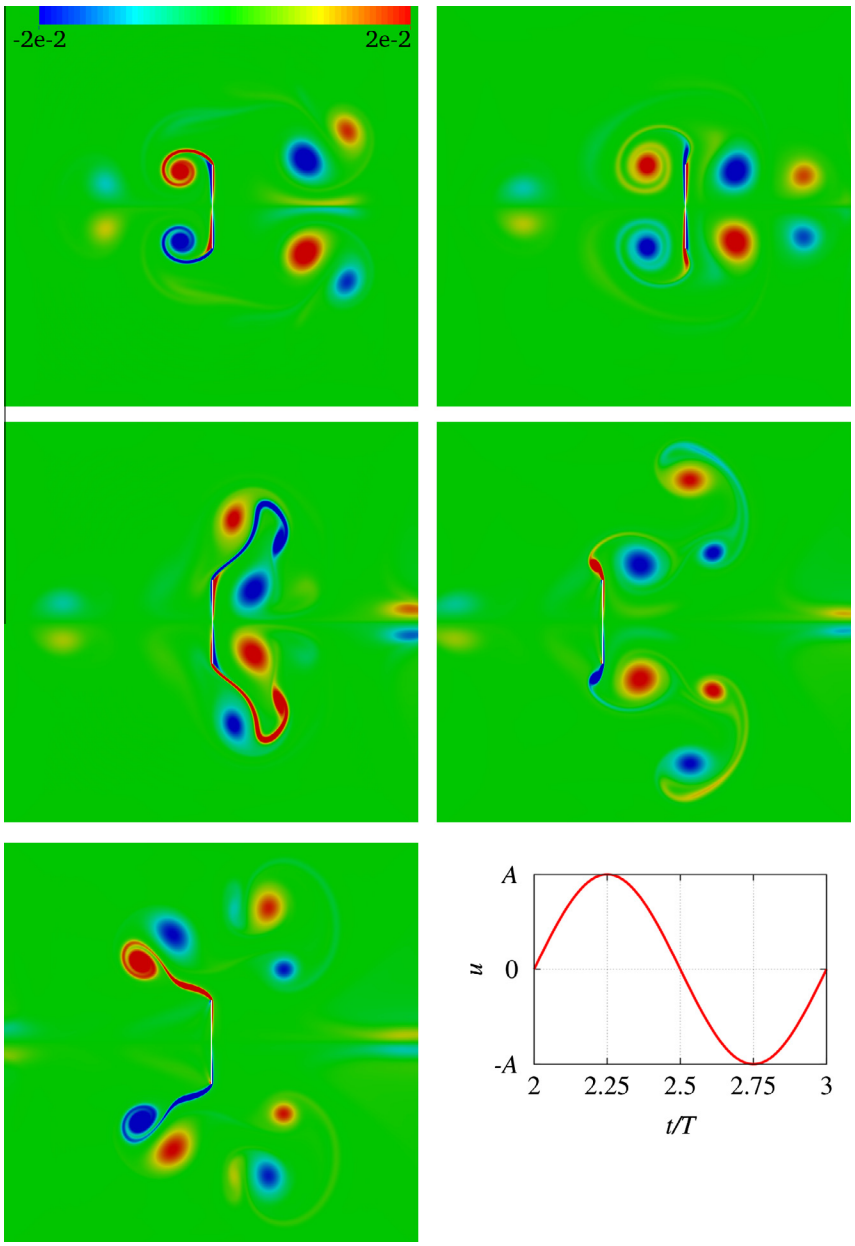

Fig. 4. Induced flow for $\varepsilon = 0.5$ and $\beta = 300$. The vorticity field at different time instants: $t/T = 2$ (top left), $t/T = 2.25$ (top right), $t/T = 2.5$ (mid left), $t/T = 2.75$ (mid right) and $t/T = 3$ (bottom left). The colormap is kept fixed for all the graphs and its range is reported only in the top left panel. The time history of the lamina's displacement is recalled in the bottom right panel, where A is the amplitude. (For interpretation of the references to color in this figure legend, the reader is referred to the web version of this article.)

independent of the underlying fluid lattice avoids oscillation-dependent activation/desactivation of fluid nodes, *i.e.* the switch of lattice nodes from solid to fluid (and vice versa) following the displacement of the lamina. Therefore, no refill procedures are necessary, which can lead to the violation of the mass conservation in the system. Secondly, the forces acting upon the immersed solid are readily and simply available, thus skipping the implementation and the usage of additional stress-integration procedures, which can severely affect the computational performance. Finally, the use of the IB method yields a LB algorithm that is numerically more stable. Therefore, lower values of the relaxation parameter τ are permitted [55]. This means in particular that, for a given lattice resolution and Reynolds number, simulations characterized by a lower viscosity can be achieved, thus allowing to select a lower reference velocity. As a consequence, the Mach number reduces and the deleterious (Mach-induced) compressibility effects annihilate as well [35].

3. Results and discussion

In this section, the numerical results are discussed. All hydrodynamic quantities are given in lattice units with Δx and Δt taken as spatial and temporal reference scales. Outflow boundary conditions have been used on the contour of the simulation domain, namely, $\mathbf{n} \cdot \nabla f_i = 0$ for all populations with $\mathbf{n}$ being the outer normal to the boundary [56]. Simulations have been carried out for values of the non-dimensional amplitude ranging from $\varepsilon = 0.05$ (small) to $\varepsilon = 0.7$ (large). The dependence on the frequency

parameter has been explored by considering the values $\beta = 50,\ 100,\ 150,\ 200,\ 250,\ 300$. The relaxation parameter has been fixed at $\tau = 0.56$ corresponding to a fluid kinematic viscosity $\nu = 0.02$. According to [15], oscillations are successfully captured if the displacement of the lamina around its initial position extends over 15 lattice nodes for moderate-amplitude oscillations. Therefore, this criterion has been respected in our simulations for $\varepsilon \leqslant 0.1$. For large-amplitude oscillations, more points have been used in order to keep a sufficiently fine resolution in the direction along the lamina, and so that the maximum velocity of the lamina did not exceed a certain threshold: $V_{\max} < 0.025$ (in lattice units). The resulting Mach number $\mathcal{M} = V_{\max}/c_s \simeq 0.043$, which alleviates the compressibility effects affecting the solution of the LB algorithm. Finally, the influence of outflow boundary conditions has been minimized by setting $H/D = 5$, as discussed in Appendix A.

3.1. Flow physics

In Fig. 3, the vorticity field is depicted at $t/T = 3$ for $\varepsilon = 0.075$ and $\varepsilon = 0.1$, which are representative of small and moderate (normalized) amplitudes, and $\beta = 100$ and $\beta = 300$, which are representative of small and large (normalized) frequencies. In agreement with the numerical results presented in [18], vorticity is generated by the tips of the lamina. As the two dimensionless parameters grow, the fluid domain affected by the motion of the lamina extends. However, for these values of the parameters the vortical structures generated by the displacement of the lamina remain attached to this latter. This trend is fully consistent with [15,31], where evidence is provided that the induced fluid motions progressively expands as β grows. Interestingly, the vorticity is not only located around the tips of the lamina but on the whole surface, vanishing close to the middle of the lamina.

The expansion of vortex structures is amplified when considering large-amplitude oscillations, *i.e.* for $\varepsilon > 0.1$. In Fig. 4, the vorticity field is displayed for $\varepsilon = 0.5$ and $\beta = 300$ at different time instants covering a whole time cycle. As time progresses, the harmonic motion of the lamina generates compelling vortex structures. Here, the flow field is far from reflecting the harmonic displacement of the lamina. In this regime, vortices are generated and detach from the lamina at a much higher rate than they are dissipated. Therefore, successive vortices can interact with each other and with the lamina, in a non-trivial manner. At $t/T = 2$, the rightward motion of the lamina generates two vortices in its wake (on the left). On its right, the lamina interacts with the four vortices that have been created during the previous time cycle. Then, the newly produced vortices are sucked up on the right,

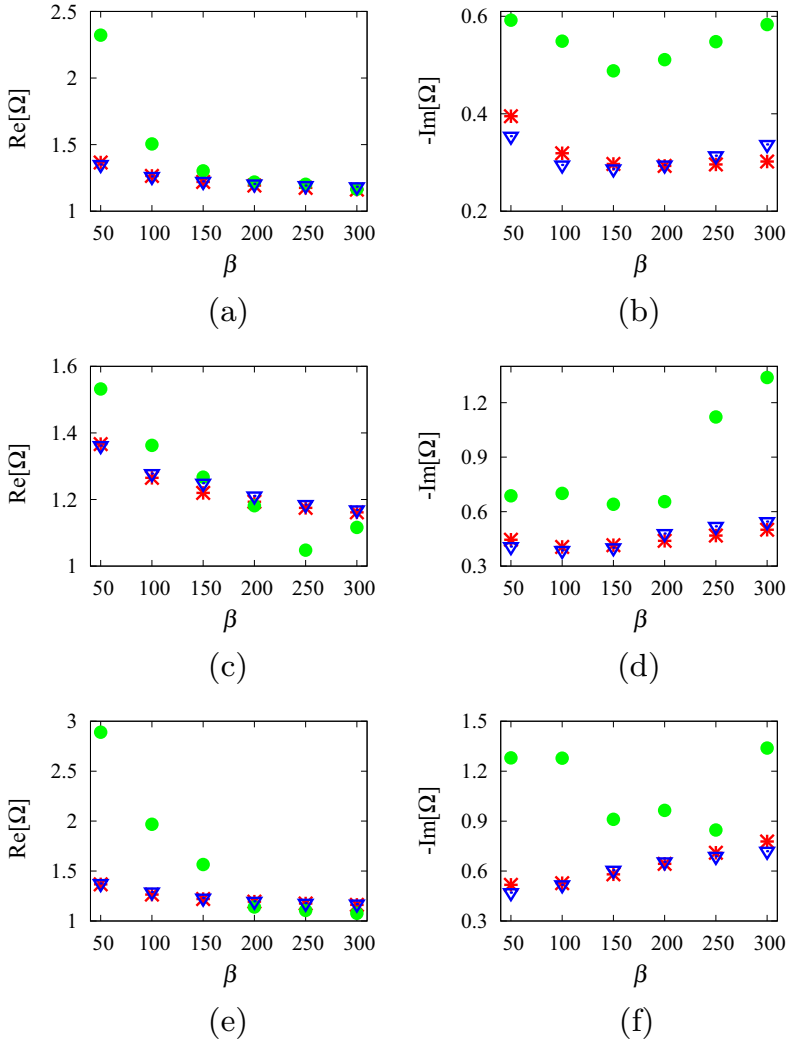

Fig. 5. The real and imaginary parts of the hydrodynamic function for different values of β at $\varepsilon = 0.05$ (top row), $\varepsilon = 0.075$ (mid row) and $\varepsilon = 0.1$ (bottom row). Comparisons between the empirical solution proposed by [31] (red asterisks), previous LB simulations by [15] (green circles) and the present LB simulations (blue inverted triangles). (For interpretation of the references to color in this figure legend, the reader is referred to the web version of this article.)

while the lamina is moving leftward, so that all vortices are eventually located on the right of the lamina at $t/T = 2.75$. When the motion reverses, the lamina faces the previously shed vortices. The sharp tips of the lamina then induce new vortex structures which largely develop up to $t/T = 3$, and so on. This scenario illustrates the typical (complex) mechanism of interaction between the vortices themselves and the oscillating lamina. Our observation corroborates the results reported very recently in [18], where analogous vorticity patterns are shown in smoothed particle hydrodynamic (SPH) simulations. However, unlike [18], the vorticity field is here not notably affected by numerical noise.

In this large-amplitude regime, a complex time-dependent flow organizes around the lamina. This induced flow drastically influences the hydrodynamic load experienced by the lamina. A quantitative characterization of this hydrodynamic load is now presented, with a specific focus on its main component at the characteristic frequency $1/T$.

3.2. Hydrodynamic function

In the frequency domain, the main component (at frequency $1/T$) of the horizontal force acting upon the lamina can be written as

$$\hat{F}(T) = \frac{\pi}{4}\rho\left(\frac{2\pi}{T}\right)^2 D^2 A\Omega(\varepsilon,\beta), \tag{11}$$

where Ω refers to the so-called (complex-valued) *hydrodynamic function*. In practice, the force F is computed according to Eq. (10) and is expressed in physical units (N/m) by setting $\rho = 10^3$ kg/m^3. The hydrodynamic function can be decomposed into a real and an imaginary part:

$$\Omega(\varepsilon,\beta) = \frac{\hat{F}(T)}{\frac{\pi}{4}\rho\left(\frac{2\pi}{T}\right)^2 D^2 A} = \mathrm{Re}[\Omega] + i\,\mathrm{Im}[\Omega], \tag{12}$$

where i is the imaginary unit ($i^2 = -1$). These two parts are estimated by fitting $F(t)$ with a sine function $F_0\sin(2\pi t/T + \phi)$; the fit relies on a (non-linear) least-square method [32]. The first cycle of oscillation is neglected to avoid possible dependence on the initial transient dynamics. Then, two subsequent cycles are analyzed to estimate the amplitude F_0 and the phase ϕ in order to obtain $\mathrm{Re}[\Omega] = \Omega_0\cos\phi$ and $\mathrm{Im}[\Omega] = \Omega_0\sin\phi$ with $\Omega_0 = F_0/\left(\pi/4\rho(2\pi/T)^2 D^2 A\right)$ according to Eq. (12). These two quantities are directly proportional to the added mass and non-linear damping effects, respectively [30].

In Fig. 5, the real and imaginary parts of Ω are displayed for different parameters. Our interest is on moderate oscillation amplitudes, *i.e.* $\varepsilon \leqslant 0.1$. The results are compared with the ones obtained by [15] in a previous study carried out within the LB framework, and with the empirical law (based on experimental measurements) proposed by [31]:

$$\mathrm{Re}[\Omega] = 1.02 + 2.45\beta^{-0.5}, \tag{13}$$

$$\mathrm{Im}[\Omega] = -2.49\beta^{-0.5} - 0.879\beta^{0.75}\varepsilon^2. \tag{14}$$

The first equation corresponds to the added mass computed by Sader in the limit of vanishing amplitude, whereas the second equation encompasses an additional term in ε^2 to account for moderate oscillation amplitudes. The present results agree very well with this (empirical) law for both $\mathrm{Re}[\Omega]$ and $\mathrm{Im}[\Omega]$. It is worth noticing that the real part indeed decreases as β grows, independently of the dimensionless amplitude. The ability to capture the trend of the imaginary part is emphasized in Fig. 5(d). Specifically, in agreement with [31] it firstly decreases up to $\beta = 100$ and then increases. This specific behavior had not been captured in the previous LB simulations by [15]. For clarity, the exact values of the present results, and the reference experimental and numerical data, are reported in Tables 1 and 2 for the real and imaginary parts of the hydrodynamic function, respectively.

The accuracy of our results can be quantified by estimating the relative discrepancy with respect to the empirical prediction proposed by [31]. Precisely, this relative error is given (in percentage)

Table 1
The real part of the hydrodynamic function, $\mathrm{Re}[\Omega]$, for moderate oscillation amplitudes. Comparisons between the experimental results (independent of ε) obtained by [31] (exp.), the numerical results from a previous LB simulation by [15] (num.) and the present simulations (LB–IB).

		$\beta = 50$	$\beta = 100$	$\beta = 150$	$\beta = 200$	$\beta = 250$	$\beta = 300$
	Exp.	1.366	1.265	1.220	1.193	1.175	1.162
$\varepsilon = 0.05$	Num.	2.322	1.505	1.303	1.219	1.202	1.165
	LB–IB	1.351	1.261	1.224	1.205	1.193	1.184
$\varepsilon = 0.075$	Num.	1.532	1.363	1.267	1.181	1.048	1.116
	LB–IB	1.361	1.276	1.244	1.227	1.205	1.190
$\varepsilon = 0.1$	Num.	2.890	1.968	1.566	1.140	1.106	1.077
	LB–IB	1.372	1.293	1.255	1.224	1.199	1.179

Table 2
Minus the imaginary part of the hydrodynamic function, $-\mathrm{Im}[\Omega]$, for moderate oscillation amplitudes. Comparisons between the experimental results obtained by [31] (exp.), the numerical results from a previous LB simulation by [15] (num.) and the present simulations (LB–IB).

		$\beta = 50$	$\beta = 100$	$\beta = 150$	$\beta = 200$	$\beta = 250$	$\beta = 300$
$\varepsilon = 0.05$	Exp.	0.393	0.318	0.297	0.293	0.296	0.302
	Num.	0.592	0.549	0.489	0.512	0.548	0.583
	LB–IB	0.354	0.295	0.287	0.296	0.314	0.337
$\varepsilon = 0.075$	Exp.	0.445	0.405	0.415	0.439	0.468	0.500
	Num.	0.687	0.700	0.640	0.655	1.121	1.339
	LB–IB	0.400	0.379	0.413	0.462	0.510	0.550
$\varepsilon = 0.1$	Exp.	0.517	0.527	0.580	0.644	0.710	0.777
	Num.	1.280	1.278	0.911	0.964	0.864	1.339
	LB–IB	0.462	0.499	0.583	0.655	0.706	0.742

Table 3
Relative error (in percentage) with respect to the prediction given by [31].

		$\beta = 50$	$\beta = 100$	$\beta = 150$	$\beta = 200$	$\beta = 250$	$\beta = 300$
$\varepsilon = 0.05$	$\mathrm{Re}[\Omega]$	1.156	0.285	0.361	0.981	1.532	1.980
	$\mathrm{Im}[\Omega]$	10.131	7.313	3.664	0.874	6.143	11.527
$\varepsilon = 0.075$	$\mathrm{Re}[\Omega]$	0.410	0.901	1.926	2.833	2.545	2.419
	$\mathrm{Im}[\Omega]$	10.179	6.550	0.633	5.277	8.852	9.903
$\varepsilon = 0.1$	$\mathrm{Re}[\Omega]$	0.432	2.189	2.836	2.606	2.043	1.532
	$\mathrm{Im}[\Omega]$	10.618	5.353	0.598	1.802	0.629	4.594

Table 4
Recovery of the zero-amplitude solution. Comparisons between the analytical prediction derived by [30] (theo.) and the present results (LB–IB). The relative error (in percentage) is given in the third row.

		$\beta = 50$	$\beta = 100$	$\beta = 150$	$\beta = 200$	$\beta = 250$	$\beta = 300$
$\mathrm{Re}[\Omega]$	Theo.	1.366	1.265	1.220	1.193	1.175	1.162
	LB–IB	1.361	1.277	1.231	1.219	1.199	1.184
	Error (%)	0.763	0.949	0.902	2.162	2.043	1.937
$\mathrm{Im}[\Omega]$	Theo.	0.352	0.249	0.203	0.176	0.157	0.144
	LB–IB	0.305	0.223	0.200	0.188	0.176	0.160
	Error (%)	13.273	10.442	1.628	7.060	11.697	11.297

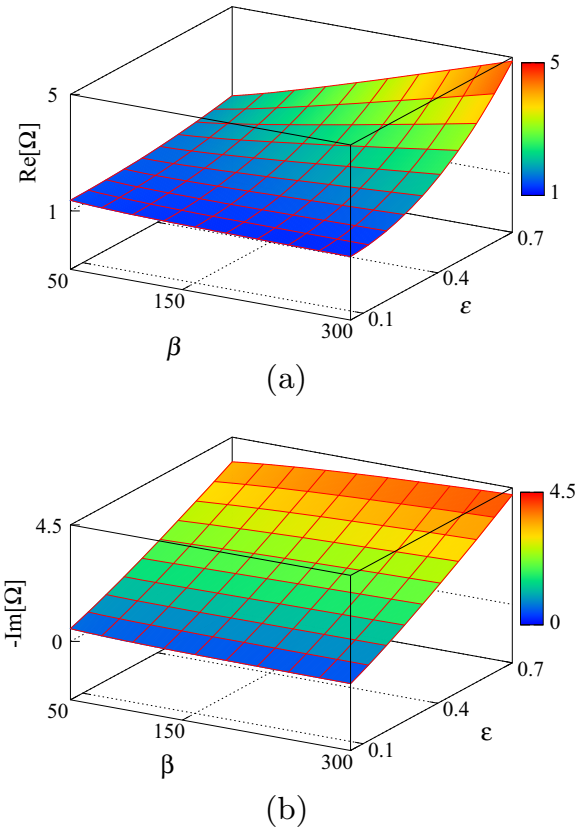

Fig. 6. Dependence on β and ε of the real and imaginary parts of the hydrodynamic function.

by $100 \times |\bar{x}_k - x_k|/|\bar{x}_k|$, where the superimposed bar identifies the reference values. It is reported in Table 3.

On the one hand, the accuracy on the added mass effect (Re[Ω]) remains high with a peak value of the error at 2.84%. This error does not vary much among the different settings (ε, β) indicating that this effect does not depend strongly on the parameters (ε, β), and that it is well captured by our numerical simulations. On the other hand, a satisfactory but lower performance is experienced for the prediction of the non-linear damping effect (Im[Ω]). This latter is more sensitive to the accurate description of the flow physics [18,31]. The largest discrepancies are observed for the extremal values of β, *i.e.* for $\beta = 50$ and $\beta = 300$. At $\beta = 50$, the induced vorticity remains concentrated in the vicinity of the lamina tips, which would require a finer spatial resolution in these regions. In this regard, grid refinement around the tips would have certainly helped to improve the accuracy. Discrepancies at $\beta = 300$ are rather interpreted as the consequence of the weak compressibility of the LB model and the related growth of higher harmonics. Nevertheless, despite these deficiencies our results exhibit relative errors considerably lower than those reported by [15].

Another assessment of our results can be achieved by extrapolating Re[Ω] and Im[Ω] to $\varepsilon = 0$, and by comparing these values with the analytical formula obtained by [30]. In practice, a linear and quadratic extrapolation have been considered for Re[Ω] and Im[Ω] respectively. The different results are summarized in Table 4. In general, the agreement with the analytical Sader's solution is again very satisfactory.

The good accuracy of our simulations for small and moderate amplitudes, encourages us to extend the characterization of the hydrodynamic function to the regime of large amplitudes, *i.e.* for $0.1 \leqslant \varepsilon \leqslant 0.7$. For consistency with the original formulation by [30], we suggest to account for the whole (ε, β) dependence of

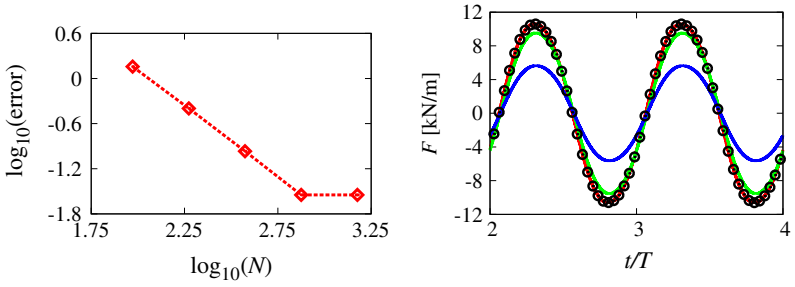

(a) Convergence analysis. (b) Boundary influence.

Fig. 7. Grid-sensitivity analysis. (a) The logarithm of the relative error versus the logarithm of the number of lattice nodes in the fluid domain, *N*. A convergence rate equal to 1.85 is obtained. (b) Boundary influence. Time history of the force for $H/D = 3$ (blue), 4 (green), 5 (red) and 6 (black circles). The solution with $H/D = 5$ overlaps with the solution with $H/D = 6$. (For interpretation of the references to color in this figure legend, the reader is referred to the web version of this article.)

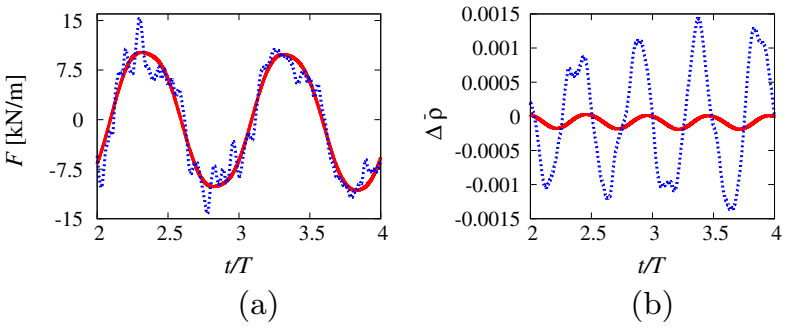

Fig. 8. Two different treatments of the boundary condition at the limit of the fluid domain: $\mathbf{n} \cdot \nabla f_i = 0$ (red continuous curve) and the "equilibrium boundary condition" (blue dashed curve). (a) Time history of the horizontal component of the force (experienced by the lamina). (b) Time history of the relative averaged mass density. (For interpretation of the references to color in this figure legend, the reader is referred to the web version of this article.)

the real and imaginary parts of the hydrodynamic function by an empirical law of the form

$$\mathrm{Re}[\Omega] = 1.02 + 2.45\beta^{-0.5} + a_R\beta^{b_R}\varepsilon^{c_R} \tag{15}$$

$$\mathrm{Im}[\Omega] = -2.49\beta^{-0.5} + a_I\beta^{b_I}\varepsilon^{c_I} \tag{16}$$

The unknown coefficients $a_R,\ b_R,\ c_R,\ a_I,\ b_I,\ c_I$ have been evaluated by a non-linear least-square method [57] yielding a coefficient of determination close to 0.98 (indicating how well the data fits the model). The resulting law writes

$$\mathrm{Re}[\Omega] = 1.02 + 2.45\beta^{-0.5} + 0.027\beta\varepsilon^{2.145}, \tag{17}$$

$$\mathrm{Im}[\Omega] = -2.49\beta^{-0.5} - 2.852\beta^{0.137}\varepsilon^{1.18}. \tag{18}$$

These equations generalizes to all amplitudes, ranging from zero to large values, the added mass and non-linear damping effects experienced by the oscillating lamina. In Fig. 6, the real and imaginary parts of $\Omega(\varepsilon,\beta)$ are plotted as a function of ε and β. For $\varepsilon > 0.1$, $\mathrm{Re}[\Omega]$ shows a dependence on the amplitude that corroborates the experimental results in [14,32]. Concerning the imaginary part, our results are consistent with [14,18,20,31,32], where a monotonic dependence of $\mathrm{Im}[\Omega]$ on ε has already been highlighted.

4. Conclusions

Combined LB–IB simulations have been successfully carried out to address the computation of the hydrodynamic load (at main frequency) acting a lamina undergoing transverse harmonic oscillations in a viscous quiescent fluid. The consistency and the good level of accuracy of the numerical approach have been carefully assessed through extensive comparisons with analytical, numerical and experimental data. In particular, it has been possible to suitably capture the mechanism of interaction between the vortices and the oscillating lamina in the regime of large amplitudes ($\varepsilon > 0.1$), and provide an extended characterization of the hydrodynamic function (at mean frequency) over the whole range of oscillation amplitudes. Within the LB framework, the present approach achieves a significant progress with respect to a previous attempt by [15]. Finally, we believe that beyond this specific application, the adopted numerical scheme, combining the LB and IB methods, provides a reliable path to the development of accurate simulations involving fluid–structure interaction phenomena. In particular, the problem of deformable oscillating bodies would be another topic of special interest.

Acknowledgments

The authors would like to thank Prof. Stefano Ubertini, Prof. Francesco Ubertini and Dr. Andrea Luigi Facci for useful and motivating discussions. A.D.R. is also grateful to Prof. Matteo Aureli and Prof. Maurizio Porfiri, who stimulated the present work.

Appendix A. Grid-sensitivity analysis

The configuration $\varepsilon = 0.1$ and $\beta = 100$ has been selected to achieve a grid-sensitivity analysis. Firstly, the convergence rate of the results is examined with respect to the grid resolution. Specifically, the imaginary part of the hydrodynamic function, $\mathrm{Im}[\Omega]$, is computed for increasingly refined grids, and the solution is compared to the reference prediction given by [31]. In Fig. 7(a), the related relative error is plotted against the number of lattice nodes in the fluid domain, N. The error decreases rapidly as $N^{-1.85}$, until it reaches a plateau for $N > 750$. Accordingly, $N = 750$ has been selected for all simulations in order to obtain an optimal balance between the accuracy and the computational cost. Secondly, the influence of the outflow boundary is investigated. In particular, different ratii between the size of the domain, H, and the length of the lamina, D, are considered, namely, $H/D = 3,\ 4,\ 5,\ 6$. In Fig. 7b, the time history of the force is depicted for the various ratii H/D. It appears that the solution has mainly converged for $H/D \geqslant 5$. Accordingly, all simulations have been carried with $H/D = 5$.

As already mentioned, the LB method is second-order accurate in space and time (with respect to the Navier–Stokes equations). In order to preserve this property, sufficiently accurate boundary conditions need to be implemented, otherwise, the whole solution deteriorates. In this paper, outflow boundary conditions have been used by imposing $\mathbf{n}\cdot\nabla f_i = 0$ at the domain frontier. An alternative condition would have been to impose a null velocity gradient at the boundary by enforcing an equilibrium distribution (at the boundary). In Fig. 8(a), the time history of the horizontal component of the force experienced by the lamina is plotted for these two different boundary treatments. The force resulting from the "equilibrium boundary condition" shows a signal highly affected by noise, whereas $F(t/T)$ remains smooth as expected for the $\mathbf{n}\cdot\nabla f_i = 0$ condition. Another difference between these two boundary conditions is provided by considering the temporal evolution of the (relative) averaged mass density $\Delta\bar{\rho}(t)$ (see Fig. 8(b)). This quantity is computed as

$$\Delta\bar{\rho}(t) = \frac{\bar{\rho}(t) - \bar{\rho}(0)}{\bar{\rho}(0)}, \tag{19}$$

where $\bar{\rho}(t) = \sum_{\boldsymbol{x}}\rho(\boldsymbol{x},t)/N$ denotes the average value of the mass density at time t. One can immediately observe that the $\mathbf{n}\cdot\nabla f_i = 0$ condition better ensures the conservation of mass.

References

[1] Ellington CP. The novel aerodynamics of insect flight: applications to micro-air vehicles. J Exp Biol 1999;202:3439–48.
[2] Shyy W, Berg M, Ljungqvist D. Flapping and flexible wings for biological and micro air vehicles. Prog Aerospace Sci 1999;35:455–505.
[3] Ettinger SM, Nechyba MC, Ifju PG, Waszak M. Vision-guided flight stability and control for micro air vehicles. Adv Robot 2003;17:617–40.
[4] Ansari S, Abikowski R, Knowles K. Aerodynamic modelling of insect-like flapping flight for micro air vehicles. Prog Aerospace Sci 2006;42:129–72.
[5] Shyy W, Aono H, Chimakurthi SK, Trizila P, Kang C-K, Cesnik CE, et al. Recent progress in flapping wing aerodynamics and aeroelasticity. Prog Aerospace Sci 2010;46:284–327.
[6] Orlowski CT, Girard AR. Dynamics, stability, and control analyses of flapping wing micro-air vehicles. Prog Aerospace Sci 2012;51:18–30.
[7] Aureli M, Prince C, Porfiri M, Peterson SD. Energy harvesting from base excitation of ionic polymer metal composites in fluid environments. Smart Mater Struct 2010;19:015003.
[8] Giacomello A, Porfiri M. Underwater energy harvesting from a heavy flag hosting ionic polymer metal composites. J Appl Phys 2011;109:084903.
[9] Erturk A, Delporte G. Underwater thrust and power generation using flexible piezoelectric composites: an experimental investigation toward self-powered swimmer-sensor platforms. Smart Mater Struct 2011;20:125013.
[10] Lu C, He Y, Wu G. Coupled analysis of nonlinear interaction between fluid and structure during impact. J Fluids Struct 2000;14:127–46.
[11] Qin Z, Batra R. Local slamming impact of sandwich composite hulls. Int J Solids Struct 2009;46:2011–35.
[12] Abrate S. Hull slamming. Appl Mech Rev 2011;64:060803.
[13] Panciroli R, Shams A, Porfiri M. Experiments on the water entry of curved wedges: high speed imaging and particle image velocimetry. Ocean Eng 2015;94:213–22.
[14] Bidkar RA, Kimber M, Raman A, Bajaj AK, Garimella SV. Nonlinear aerodynamic damping of sharp-edged flexible beams oscillating at low Keulegan–Carpenter numbers. J Fluid Mech 2009;634:269–89.
[15] Falcucci G, Aureli M, Ubertini S, Porfiri M. Transverse harmonic oscillations of laminae in viscous fluids: a lattice Boltzmann study. Philos Trans Roy Soc – Ser A 2011;369:2456–66.
[16] Facci AL, Porfiri M. Nonlinear hydrodynamic damping of sharp-edged cantilevers in viscous fluids undergoing multi-harmonic base excitation. J Appl Phys 2012;112:124908.
[17] Facci AL, Porfiri M. Analysis of three-dimensional effects in oscillating cantilevers immersed in viscous fluids. J Fluids Struct 2013;38:205–22.
[18] Tafuni A, Sahin I. Non-linear hydrodynamics of thin laminae undergoing large harmonic oscillations in a viscous fluid. J Fluids Struct 2015;52:101–17.

[19] Tuck E. Calculation of unsteady flows due to small motions of cylinders in a viscous fluid. J Eng Math 1969;3:29–44.
[20] Graham J. The forces on sharp-edged cylinders in oscillatory flow at low Keulegan–Carpenter numbers. J Fluid Mech 1980;97:331–46.
[21] Bearman P, Downie M, Graham J, Obasaju E. Forces on cylinders in viscous oscillatory flow at low Keulegan–Carpenter numbers. J Fluid Mech 1985;154:337–56.
[22] Sarpkaya T. Force on a circular cylinder in viscous oscillatory flow at low Keulegan–Carpenter numbers. J Fluid Mech 1986;165:61–71.
[23] Van Eysden CA, Sader JE. Frequency response of cantilever beams immersed in compressible fluids with applications to the atomic force microscope. J Appl Phys 2009;106:094904.
[24] De Rosis A, Falcucci G, Ubertini S, Ubertini F. Aeroelastic study of flexible flapping wings by a coupled lattice Boltzmann finite element approach with immersed boundary method. J Fluids Struct 2014;49:516–33.
[25] Intartaglia C, Soria L, Porfiri M. Hydrodynamic coupling of two sharp-edged beams vibrating in a viscous fluid. Proc Roy Soc A: Math Phys Eng Sci 2014;470:20130397.
[26] Green CP, Sader JE. Frequency response of cantilever beams immersed in viscous fluids near a solid surface with applications to the atomic force microscope. J Appl Phys 2005;98:114913.
[27] Grimaldi E, Porfiri M, Soria L. Finite amplitude vibrations of a sharp-edged beam immersed in a viscous fluid near a solid surface. J Appl Phys 2012;112:104907.
[28] De Rosis A. Harmonic oscillations of a lamina in a viscous fluid near a solid surface: a lattice Boltzmann-immersed boundary approach. Phys A: Stat Mech Appl 2014;415:386–97.
[29] De Rosis A. Harmonic oscillations of laminae in non-Newtonian fluids: a lattice Boltzmann-immersed boundary approach. Adv Water Resour 2014;73:97–107.
[30] Sader JE. Frequency response of cantilever beams immersed in viscous fluids with applications to the atomic force microscope. J Appl Phys 1998;84:64–76.
[31] Aureli M, Basaran M, Porfiri M. Nonlinear finite amplitude vibrations of sharp-edged beams in viscous fluids. J Sound Vib 2012;331:1624–54.
[32] Aureli M, Porfiri M. Low frequency and large amplitude oscillations of cantilevers in viscous fluids. Appl Phys Lett 2010;96:164102.
[33] Higuera FJ, Succi S, Benzi R. Lattice gas dynamics with enhanced collisions. Europhys Lett 1989;9:345–9.
[34] Benzi R, Succi S, Vergassola M. The lattice Boltzmann equation: theory and applications. Phys Rep 1992;222:145–97.
[35] Succi S. The lattice Boltzmann equation for fluid dynamics and beyond. Clarendon; 2001.
[36] Chen H, Chen S, Matthaeus WH. Recovery of the Navier–Stokes equations using a lattice-gas Boltzmann method. Phys Rev Lett 1992;45:R5339–42.
[37] Fadlun E, Verzicco R, Orlandi P, Mohd-Yusof J. Combined immersed-boundary finite-difference methods for three-dimensional complex flow simulations. J Comput Phys 2000;161:35–60.
[38] Peskin C. The immersed boundary method. Acta Numerica 2002;11:479–517.
[39] Luo K, Wang Z, Fan J. A modified immersed boundary method for simulations of fluid–particle interactions. Comput Methods Appl Mech Eng 2007;197:36–46.
[40] Le D, Khoo B, Lim K. An implicit-forcing immersed boundary method for simulating viscous flows in irregular domains. Comput Methods Appl Mech Eng 2008;197:2119–30. Immersed boundary method and its extension.
[41] Wu J, Shu C. Implicit velocity correction-based immersed boundary-lattice Boltzmann method and its applications. J Comput Phys 2009;228:1963–79.
[42] Sotiropoulos F, Yang X. Immersed boundary methods for simulating fluid–structure interaction. Prog Aerospace Sci 2014;65:1–21.
[43] Feng Z-G, Michaelides EE. The immersed boundary-lattice Boltzmann method for solving fluid-particles interaction problems. J Comput Phys 2004;195:602–28.
[44] Sui Y, Chew Y-T, Roy P, Low H-T. A hybrid immersed-boundary and multi-block lattice Boltzmann method for simulating fluid and moving-boundaries interactions. Int J Numer Methods Fluids 2007;53:1727–54.
[45] Zhu L, He G, Wang S, Miller L, Zhang X, You Q, et al. An immersed boundary method based on the lattice Boltzmann approach in three dimensions, with application. Comput Math Appl 2011;61:3506–18.
[46] Kruger T, Varnik F, Raabe D. Efficient and accurate simulations of deformable particles immersed in a fluid using a combined immersed boundary lattice Boltzmann finite element method. Comput Math Appl 2011;61:3485–505.
[47] De Rosis A. A lattice Boltzmann model for multiphase flows interacting with deformable bodies. Adv Water Resour 2014;73:55–64.
[48] Favier J, Revell A, Pinelli A. Numerical study of flapping filaments in a uniform fluid flow. J Fluids Struct 2015;53:26–35. Special Issue on Unsteady separation in fluid–structure interaction-I.
[49] Guo Z, Zheng C, Shi B. Discrete lattice effects on the forcing term in the lattice Boltzmann method. Phys Rev E 2002;65:046308.
[50] Favier J, Revell A, Pinelli A. A lattice Boltzmann-immersed boundary method to simulate the fluid interaction with moving and slender flexible objects. J Comput Phys 2014;261:145–61.
[51] Filippova O, Hänel D. Lattice Boltzmann simulation of gas-particle flow in filters. Comput Fluids 1997;26:697–712.
[52] Mei R, Luo L, Shyy W. An accurate curved boundary treatment in the lattice Boltzmann method. J Comput Phys 1999;155:307–30.
[53] Mei R, Yu D, Shyy W, Luo L. Force evaluation in the lattice Boltzmann method involving curved geometry. Phys Rev Lett E 2002;65:041203.
[54] De Rosis A, Falcucci G, Porfiri M, Ubertini F, Ubertini S. Hydroelastic analysis of hull slamming coupling lattice Boltzmann and finite element methods. Comput Struct 2014;138:24–35.
[55] De Rosis A, Ubertini S, Ubertini F. A comparison between the interpolated bounce-back scheme and the immersed boundary method to treat solid boundary conditions for laminar flows in the lattice Boltzmann framework. J Sci Comput 2014;61:477–89.
[56] Suzuki K, Inamuro T. Effect of internal mass in the simulation of a moving body by the immersed boundary method. Comput Fluids 2011;49:173–87.
[57] MATLAB. Version 7.10.0 (R2010a). The MathWorks Inc., Natick, Massachusetts; 2010.